High-valent metal site incorporated heterointerface catalysts for high-performance anion-exchange membrane water electrolysers

Gwan Hyun Choi [a,b,1], N. Clament Sagaya Selvam [a,c,1], Hyunwoo Kim [d], Young Sang Park [b,e], Jiyoon Jung [b,e], Myeong Gyun Nam [a], Hyo Sang Jeon [f], Albert S. Lee [b,e,*], Won-Sub Yoon [d,g,**], Pil J. Yoo [a,g,h,***]

[a] School of Chemical Engineering, Sungkyunkwan University (SKKU), Suwon 16419, Republic of Korea
[b] Materials Architecting Research Center, Korea Institute of Science and Technology (KIST), Seoul 02792, Republic of Korea
[c] Department of Chemistry, State University of New York at Binghamton, Binghamton, NY 13902, United States
[d] Department of Energy Science, Sungkyunkwan University (SKKU), Suwon 16419, Republic of Korea
[e] Convergence Research Center for Solutions to Electromagnetic Interference in Future-mobility, Korea Institute of Science and Technology (KIST), Seoul 02792, Republic of Korea
[f] Technological Convergence Center, Korea Institute of Science and Technology (KIST), Seoul 02792, Republic of Korea
[g] SKKU Institute of Energy Science and Technology (SIEST), Sungkyunkwan University (SKKU), Suwon 16419, Republic of Korea
[h] SKKU Advanced Institute of Nanotechnology (SAINT), Sungkyunkwan University (SKKU), Suwon 16419, Republic of Korea

ARTICLE INFO

ABSTRACT

The design of heterointerface-structured catalysts with tunable active sites is critical to address the activity and durability challenges of water oxidation process. In this study, a novel interfacial engineering strategy based on the anionic diffusion-limited Kirkendall effect (KE) was employed for the synthesis of a FeCo/FeCoP with high-valent Fe ($Fe^{+3.18}$) sites. Specifically, a model system of the FeCo/FeCoP heterointerface was obtained through the phosphidation of carbon-encapsulated FeCo nanoparticles. The highly efficient and stable oxygen evolution reaction (OER) performance of the FeCo/FeCoP catalyst was demonstrated in an anion-exchange membrane water electrolyser (12.26 A cm^{-2} at 2.0 V). Through density functional theory calculations, the high-valent Fe sites in the FeCo/FeCoP heterointerface were found to balance the adsorption energetics of the OER intermediates. The structure–oxidation state–OER activity correlation of the FeCo/FeCoP catalysts demonstrated herein emphasises the significance of understanding the water oxidation chemistry of heterointerface-structured catalysts for their potential applications in different energy conversion devices.

1. Introduction

The anodic oxygen evolution reaction (OER) in alkaline electrocatalytic water splitting suffers from sluggish kinetics as it involves the transfer of four electrons ($4\,OH^- \leftrightarrow O_2 + 2\,H_2O + 4e^-$) [1–3]. Fe-doped Ni/Co-based electrocatalysts, such as $Ni(Fe)O_xH_y$ and $Co(Fe)O_xH_y$, exhibit superior OER performance to that of the noble metal-based (Ir and Ru) benchmark OER electrocatalysts [4–8]. The critical role of the Fe species in enhancing the OER performance of the Ni/Co-based catalysts has been investigated through experimental in situ and operando analyses as well as density functional theory (DFT) calculations. The valence state of Fe can regulate the energetics of the OER intermediates predominantly; for instance, the theoretical overpotential of the high-valent Fe sites (Fe–O) is comparatively lower than those of the Ni/Co active sites (M–O, M = Ni, Co) [4,5,9]. Electrodeposition is commonly employed to incorporate high-valence Fe sites into host catalyst systems and consequently establish heterointerface structures with a uniform active site distribution [9]. Other methods, such as precipitation and sol–gel synthesis, have also been utilized to produce a wide variety of high performance OER electrocatalysts with

high-valence transition metal modulators [10]. Finally, designing catalysts with high-valence metallic sites is an efficient strategy to achieve considerably improved OER activity.

Surface/interface engineering is a promising approach to enhance the performance of electrocatalysts toward OER [11–13]. Due to the presence of two distinct catalyst surfaces at the interface, it has also been widely utilized as a bifunctional catalyst for water splitting [14–17]. Particularly, modifying the heterogeneous interface of a catalyst can modulate its electronic structure and the corresponding interfacial charge-transfer characteristics [18,19]. For instance, Suryanto et al. confirmed that the significantly improved OER performance of Ni/Fe$_2$O$_3$ with respect to that of a physical mixture of Ni/Fe or Ni/Fe alloy nanoparticles (NPs) can be attributed to the presence of active sites at its interface [20]. Similarly, other combinations of heterogeneous interface structures, such as Co$_3$O$_4$/FeCoP or Co/Ni$_3$N, exhibited favorable adsorption energies for the reaction intermediates at the interfacial active sites [21,22]. However, the unsatisfactory coordination/valency sites of atoms at the interface, which is generated by the mismatch in lattice parameters, can cause a marked difference in the adsorption characteristics of the reaction intermediates and limit the OER performance [23]. Despite the reported improvements in the OER performance through heterogeneous interfacial engineering, the correlation between the valence state of the metal sites at the heterointerface and the corresponding OER activity is yet to be established. Furthermore, novel design and synthesis strategies to produce heterointerface structures with high-valence metal sites are required to address the inconsistent OER activity and to fully understand the underlying structure–performance relationship of the catalyst.

The Kirkendall effect (KE)-induced interfacial modification has been developed as an efficient method to tune the active sites of the catalyst to improve its OER performance [24,25]. The KE is based on the disparity between the diffusion rates of different elements within a single particle [26,27]. Considering this effect, the asymmetric diffusion of the core atoms to the surface is preferentially driven by the reaction with surface-bound reactant molecules. As a result, a void in the core is simultaneously formed with a second phase at the surface of the shell. KE has been employed primarily to generate hollow core-laden particles with highly tunable electrocatalytic performance [28]. However, when the degree of the reaction is regulated by controlling the outward diffusion rate of the core atoms, that is under diffusion-limited conditions, a heterointerface structure (A/B) with residual core (A) and newly formed shell (B) phases is typically formed [29–31]. For example, particles composed of elements with low ionic diffusivities, such as Al and Zn, would exhibit different outward diffusion rates depending on the particle size during the thermal oxidation process [32]. Therefore, for larger particles, the low mobility of metal ions in their respective oxide phases inhibits the continuous growth of the external oxide layer. Incomplete oxidation eventually forms a heterointerface structure composed of a metallic core surrounded by its oxide shell.

The synthesis of heterointerface structures based on KE has already been reported [33–35]. However, designing a heterointerface with metals of different valences is beneficial for the synthesis of high-performance OER catalysts [36,37]. In general, controlling the diffusion rate at the nanoscale while simultaneously optimizing the local electronic structure of the catalyst is difficult. When two crystalline phases with different lattice parameters form an A/B heterointerface, a set of divided lattice regions is formed to relieve the stress across the interface and maintain atomic ordering [38,39]. For example, misfit dislocations may be formed wherein coherent regions with atom-by-atom matching at the interface are separated [40]. Accordingly, the atomic valency at the dislocation defect sites is likely to be unsaturated owing to the different interatomic distances, thereby imposing an unusual atomic structure with a high valence state. Studying the distinct atomic valency at the heterointerface by considering the diffusion-regulated KE is critical to establish and understand the structure–activity relationship of the OER electrocatalyst.

In this study, a novel synthesis method for the production of a heterointerface structure (FeCo/FeCoP) involving a controlled phosphidation process for FeCo NPs is demonstrated. To reduce the inward diffusion of the phosphorous gas and control the KE, a highly graphitized carbon shell was introduced over the FeCo NPs as a diffusion barrier [41]. In addition, the outward diffusion of the FeCo sites was precisely controlled by varying the size of the FeCo NPs, allowing the formation of an outer FeCoP layer. Consequently, a structurally modulated FeCo/-FeCoP/C heterointerface was successfully obtained. X-ray absorption near-edge structure (XANES) analysis revealed the presence of Fe and Co with distinct oxidation states at the interface (Fe$^{+3.18}$ and Co$^{+1.67}$). In contrast, the oxidation states of Fe and Co at the interface of a single phase FeCoP control sample were Fe$^{+1.98}$ and Co$^{+1.19}$, respectively. The superior OER performance of the FeCo/FeCoP/C heterointerface structure relative to that of the single phase FeCoP catalyst reveals that the formation of interfacial metal atoms with higher oxidation states considerably improves the OER activity of the electrocatalyst. In addition to half-cell tests, full cell tests utilizing FeCo/FeCoP/C as an OER catalyst in an anion-exchange membrane water electrolyser (AEMWE) were performed. The recorded current density at a cell voltage of 2.0 V was as high as 12.26 A cm^{-2}. From DFT calculations, the key active sites that facilitated OER were the Fe species at the interface with a high oxidation state. Overall, the heterointerface structure-oxidation state––activity relationship was established systematically, which can be beneficial for the design of high-performance, heterointerface-structured OER catalysts. Therefore, the reported anion diffusion-limited KE approach for the design of the heterointerface structure in which the oxidation state of the metal centers is tuned to maximize the activity proves to be a promising method for the development of high-performance OER catalysts.

2. Experimental

2.1. Materials

Tannic acid (TA, ACS reagent, Sigma-Aldrich), cobalt chloride hexahydrate (CoCl$_2$•6 H$_2$O, ≥ 98%, Sigma-Aldrich), iron chloride hexahydrate (FeCl$_3$•6 H$_2$O, ≥ 98%, Sigma-Aldrich), sodium hypophosphite monohydrate (NaH$_2$PO$_2$•H$_2$O, ≥ 99%, Sigma-Aldrich), PtRu/ C (50 wt% Pt and 25 wt% Ru, Alfa-Aesar), ammonia solution (NH$_4$OH, 28 ~ 30%, Sigma-Aldrich), Vulcan carbon (XC-72, Nara-celtech) and KOH solution (Sigma-Aldrich) were used. All chemicals were used as received without further purification.

2.2. Synthesis of FeCo/FeCoP/C, bare FeCoP and FeCoP+XC-72

To synthesis FeCo/C precursor for phosphidation, previously reported methods were used to derive graphitic carbon shell formed on metal nanoparticles [41]. Metal-chelated TA (metal/TA) complexes were firstly prepared by simple mixing of 10 ml of metal chloride solution (molar ratio of Fe and Co = 1:1) and 10 ml of TA aqueous solution. On the basis of 0.5 g of TA dissolved in 10 ml of water (29.4 mM), solutions were mixed with desired molar complexation ratio varying from 1:20–1:0.05 (TA: hydrated metal chloride), followed by adding the ammonia solution to increase the pH to 10.5. Obtained metal/TA complexes in solution was placed on Teflon-lined autoclave and was subject to hydrothermal reaction at 180 °C for 12 h. After hydrothermal reaction, black-brownish solution containing metal-ligand complexes was washed three times with aqueous solution (deionized water) using ultra-centrifugation separation process. In order to obtain powders, the collected wet complexes after ultra-centrifugation were fully dried in vacuum at 80 °C for 3 h.

Carbonized FeCo/C were synthesized by thermal carbonization of dried complexes using electrical tube furnace (R 50/250/13, Nabertherm) at 900 °C with a ramp rate of 5 °C min^{-1} and kept for 2 h under argon-purged atmosphere. The as-synthesized FeCo/C (100 mg) was

placed at the middle of an alumina boat and 1.0 g of NaH_2PO_2 was placed at the upstream side. The alumina boat was put in a tube furnace and heated to 300 ℃ with a ramp rate of 5 ℃ min^{-1} and kept for 2.5 h under argon-purged atmosphere to yield FeCo/FeCoP/C. The bare FeCoP were prepared by following same phosphidation procedure of synthesizing FeCo/FeCoP/C, except for preparing FeCo precursor. Here, as-prepared FeCo/C were oxidized in a tube furnace at the 600 ℃ with a ramp rate of 5 ℃ min^{-1} and kept for 2 h to yield $FeCoO_x$ as a precursor for post phosphidation process. FeCoP+XC-72 samples were prepared by simply mixing FeCoP and Vulcan carbon powders with desired mass ratio.

2.3. Synthesis of trimethyl ammonium functionalized polystyrene ionomers (TMA-70) and anion-exchange membrane (AEM)

To synthesis trimethyl ammonium functionalized polystyrene ionomers (TMA-70), polyvinylbenzyl chloride (2 g) was dissolved in DMSO (60 ml), and 45% Trimethylamine aqueous solution (1.33 ml) was added. After stirring for 3 h at room temperature, add 2-(4-fluorophenyl)ethylamine (0.586 g) and stirring at 80 ℃ for 12 h. Polymer was precipitated in a mixture of tetrahydrofuran (THF) and ethyl acetate (EA) 1:1 (v/v), dissolve in methanol again, and re-precipitate in EA. The obtained powder is treated with 1 M NaOH, washed with distilled water, and vacuum dried. The obtained TMA-70 is dissolved in H_2O and IPA 1:1 (v/v) at 5 wt% to prepare an ionomeric binder solution [42].

An anion exchange membrane (AEM), XL20-rPNB-LY100, was synthesized via ring opening metathesis polymerization of norbornene as described in reference [43]. Briefly, add 0.01 g ml^{-1} Grubbs' third-generation catalyst solution in DCM to 0.01 M bromopropyl norbornene (BPNB) / DCM solution for [BPNB]:[G3] = 200:1 ratio. After stirring for 10 min, ethyl vinyl ether is added to the reaction solution and the solvent is partially evaporated. A poly(BPNB) solution is precipitated in methanol several times and dried under vacuum. After that, poly(BPNB) (0.5 g) is dissolved in toluene (62 ml) for hydrogenation of double bonds and excess tosyl hydrazide is added. The reaction is carried out under Ar gas at 110 °C for 24 h, washed several times with a saturated sodium bicarbonate solution, and then precipitated in methanol after removing toluene. To crosslinking and quaternization of the polymer, hydrogenated polymer (0.6 g) and cross-linking agent N,N,N′, N′-Tetramethyl-1,6-hexanediamine (47.6 mg) were dissolved in 25 ml and 1.5 ml toluene respectively and add TMHDA solution to the polymer solution. After stirring at room temperature for 30 min, filter it using a PTFE syringe filter and pour it into a glass dish. After drying the solution at 70 °C, remove the membrane from the glass dish and immerse in 50 wt% TMA solution to quaternize the bromopropyl groups. Then, the membrane is washed with water and immersed in 1 M NaOH solution to obtain XL20-rPNB-LY100.

2.4. Materials characterizations

To analyze the molecular structure of ionomer, 700 MHz of ^1H and ^{19}F nuclear magnetic resonance equipment (NMR, AVANCEIII700, Bruker Corporation) was used. To determine the actual amount of carbon or residual carbon content in the composites, thermogravimetric analysis (TGA) (TG/DTA7300, SEICO Inst.) was employed under air or N_2 at a heating rate of 10 °C min^{-1}. Powder X-ray diffraction (XRD) patterns were obtained (D8 Focus, Bruker AXS) using Cu Kα radiation (λ = 1.5406 Å) in the 2θ range from 10° to 85° with a step size of 0.02°s^{-1}. Surface morphologies, interface structures, and chemical compositions were observed by using high-resolution transmission electron microscopy (HR-TEM, JEM-3010, JEOL) and corresponding energy dispersive X-ray spectroscopy (EDS) for elemental analysis. X-ray photoelectron spectroscopy (XPS, ESCALAB 250) and inductively coupled plasma-optical emission spectroscopy (ICP-OES, Aglient 5100) were used to determine chemical compositions. X-ray absorption spectroscopy (XAS, synchrotron radiation based measurement) experiment was conducted

in fluorescence mode at the ambient condition on 7D beamline of Pohang Light Source-II (PLS-II). The monochromatic beam was detuned (to 75% of maximum intensity for Co K-edge and to 80% for Fe edge), to eliminate higher order harmonics using Si (111) double-crystal monochromator. The spectra were calibrated with the first inflection points (i. e., Fe K-edge = 7112 eV) in the spectra of reference metal foils and normalized using Artemis program. The normalized EXAFS signal was weighted by k^3 to magnify high-energy oscillations and then Fourier-transformed in a k-range of 2.0–10.0 Å.

2.5. Electrode preparation and measurement for electrocatalytic testing

In the case of electrocatalytic measurements, catalysts were evaluated in 1 mol L^{-1} KOH solution using an electrochemical workstation (Bio-logic, VSP). The measurements were conducted by following standard protocols. Hg/HgO saturated with NaOH and carbon rod were respectively used as reference and counter electrodes. Carbon fibre paper (CFP, 1×1 cm^2) was used as the working electrode. The catalyst, polyvinylidene fluoride (PVDF, binder), and Ketjenblack (conductive agent) were mixed in a 70: 20: 10 wt ratio. 10 wt% of N-methyl-2-pyrrolidone (NMP) was added to the mixture to make a slurry. The prepared slurry was uniformly coated on CFP and dried at 80 ℃ for 12 h in a vacuum oven. The catalysts were deposited on CFP with a loading of ∼1 mg cm^{-2}. Then, the OER activities of the as-prepared electrodes were measured in 1 mol L^{-1} KOH solution using the LSV method with 95% *iR*-compensation at the scan rate of 5 mV s^{-1}. The double-layer capacitances (C_{dl}) of the catalysts were determined in the non-faradaic potential region at various scan rates of 50, 100, 150, 200, and 250 mV s^{-1}. Potentials were expressed relative to the reversible hydrogen electrode (RHE). Electrochemical impedance spectroscopy (EIS, CHI6143E, CH Instruments, Inc.) measurement were performed at 5 mV ac oscillation amplitude over the frequency range between 100 kHz and 0.01 Hz. Fitting of the impedance data settings and simulations were performed by using the Zview software. The electrochemical surface area (ECSA) was calculated using the following formula: ECSA = C_{dl}/C_s, taking C_s (specific capacitance) equal to 0.040 mF cm^{-2}, as adopted from a previous study on OER catalysts.

2.6. Electrode preparation and measurement for membrane-electrode assembly (MEA) testing

The electrolysis reaction was carried out using a specially designed 5 cm^2 anion-exchange membrane (AEM) electrolyzer. The end plates and graphite flow field for the cathode were supplied by Scribner. The catalyst inks were sprayed onto the porous transport layers (PTLs) to make porous transport electrodes (PTEs), and the OER and hydrogen evolution reaction (HER) catalysts were coated on the 5 cm^2 commercial PtTi paper and Ni foam [44], respectively. Anion exchange membrane was prepared according to previous reports [43], consisting of a quaternary ammonium-functionalized polynorbornene with 30 μm thickness and ion-exchange capacity (IEC) 3.4 mmol g^{-1}. The AEM was soaked in a 1 M KOH bath and rinsed with a copious amount of de-ionized water prior to cell testing. The ionomeric binder for both anode and cathode was TMA-70, a high IEC trimethylammonium-functionalized polystyrene ionomer following a literature report [42]. The ink formulation includes 10 wt% of TMA-70 ionomeric binder based on the catalyst amount, 10 wt% of catalyst based on the total ink amount, and a mixture of water and IPA in a volume ratio of 1:1 v/v%.

The homogenous catalyst ink solution was prepared by adding de-ionized water, ionomer (TMA-70) and catalyst powder (FeCoP catalyst for anode and PtRu/C for cathode), which was sonicated with ice for 15 min. Then isopropyl alcohol was added and sonicated for 10 min with ice. Then the slurry was sonicated for 10 min in the bath sonicator with ice. The well dispersed anode and cathode catalyst ink was sprayed onto the surface of the PtTi paper (∼2 mg_{Pt} cm^{-2} for PtRu/C) and Ni

foam (~ 1.4 mg cm^{-2}). Both the gas diffusion electrodes (GDEs) were dried at 80 °C for 2 h.

Porous transport electrodes (PTEs) were sandwiched between the AEM and assembled with Teflon gaskets into a single cell with 60 in.-pounds torque. Stainless steel bars were used as end plates, and the anode and cathode electrical supply probes connected outside of the endplate. A 500 ml tank with circulated water was used as an electrolyte reservoir. A double-headed peristaltic pump circulated the feedstock from the reservoir. The cell was tested by a Biologic SP-200 potentiostat in combination with an HCV-3048 30 A/48 V power booster. The cell was first cycled between 1.3 V and 2.0 V at 20 mV s^{-1} while flowing 1 M KOH solution on both the anode and cathode at 80 °C until the polarization curves stabilized. Then polarization curves were recorded between 1.3 and 1.8 V while flowing 1.0 M KOH solution on both the anode and cathode at 80 °C, 10 mV s^{-1}.

2.7. Characterization of ionomer and anion-exchange membrane

The thickness of the membrane was measured with a micrometer gauge. The IEC values of ionomers (or membranes) in chloride form were determined experimentally using Mohr titration. First, a 100 $\pm$ 5 mg sample of ionomers (in chloride form) was completely dissolved in 10 ml of deionized water with the aid of heating and sonication. Subsequently, the ionomer solution was titrated with 0.1 M AgNO$_3$, where K$_2$CrO$_4$ was utilized as a colorimetric indicator. The resulting experimental IEC of the ionomers was then calculated using the following equation, which expresses the value in mequiv. g^{-1} [42].

$$IEC(mequiv. g^{-1}) = (\Delta V_{AgNO3} \times C_{AgNO3}) / W_{dry} \tag{1}$$

The volume of AgNO$_3$ titrated is represented by V_{AgNO3}, C_{AgNO3} denotes the concentration of $AgNO_3$ solution, and W_{dry} is the dry mass of the ionomer. For each ionomer sample, the average IEC value was derived from the results of the two titration methods.

2.8. Determination of electrochemically active surface area (ECSA)

Cyclic voltammetry (CV) method is used to calculate the ECSA. The double-layer capacitance of the electrodes in a non-Faradaic potential region (0.1 V window about OCP) was identified from CV graph. Then, the following formula is used to calculate ECSA [45].

$$ECSA = C_{dl} / C_s \tag{2}$$

Taking C_s (specific capacitance) equal to 0.040 mF cm$^{-2}_{geometric}$, as adopted from a previous study on OER catalysts [46].

2.9. Determination of turnover frequency (TOF)

For the calculation of the per-site turnover frequency, the following formula is used [46–51].

$$TOF = \frac{\#of\ total\ oxygen\ turn\ overs / cm^2\ geometric\ area}{\#surface\ active\ sites / cm^2\ geomteric\ area} \tag{3}$$

1) The total number of oxygen turnover is calculated from the current density according to:

2) The number of active sites is calculated by following description. Since the exact oxygen binding sites are not known, here, the number of surface active sites is conservatively estimated to the total number of surface sites (including both the transition metal (Fe and Co) and P atoms as possible active sites) from the unit cell. Detail calculation of number of active sites are described in Fig. S15. In the case of FeCoP, weighted average of CoP and FeP is applied, since the exact stoichiometric number of FeCoP is determined by ICP-OES (Table S2).

3) Finally, plot of current density can be converted into a TOF plot according to:

$$TOF = \frac{(|j| * 1.5603 * 10^{15}\ \frac{\frac{O_2}{s}}{cm^2} per\ \frac{mA}{cm^2})}{\#surface\ sites \times ECSA} \tag{5}$$

2.10. Calculations of the Faradaic efficiency of oxygen products

The oxygen gas product was quantified by gas chromatography (CG, Agilent 6890 N) equipped with a thermal conductivity detector (TCD) using He (99.9999%) as the carrier gas. The GC was directly connected to the MEA for on-line analysis using a six-port valve system. The Faradaic efficiencies (FE) for oxygen product was determined by computing the areas of the GC chromatogram as indicated below:

$$i_{partial} = V \times flow\ \ rate \times \frac{nFp_o}{RT} \tag{6}$$

$$FE = \frac{i_{partial}}{i_{total}} \times 100 \tag{7}$$

The parameter V denotes the gas product's volume concentration as determined by the previous calibration of the gas chromatograph (GC), while the flow rate (ml min^{-1}) was determined using a universal flow meter (ADM 1000, Agilent Technologies). n is the number of transferred electrons for a O$_2$ product, i_{total} (mA) is a steady-state current, T represents the temperature, $F = 96485$ (A·s mol^{-1}), $p_o = 1.013$ (bar), and $R = 8.3145$ (J mol^{-1}·K^{-1}).

2.11. Density functional theory (DFT) calculations

First-principles calculations based on density functional theory (DFT) are carried out as implemented in PWSCF Quantum-Espresso package [52]. Generalized gradient approximation (GGA) functional parametrized by Perdew, Burke and Ernzerhof (PBE) is used to treat electronic exchange-correlation interactions, in conjunction with projector augmented wave (PAW) potentials. Energy cutoff value for the plane-wave basis function is set to 400 eV [53–55]. A Hubbard-U correction (DFT + U method) was applied, to improve the description of FeCo/FeCoP. For all calculations, Monkhorst-Pack k-point mesh is used [56]. Geometry optimization are done for supercell slabs, whereas a vacuum of more than 10 Å is introduced along the z-direction.

The electronic and charge properties of the adsorbates and FeCo/FeCoP systems were investigated by analyzing the Bader charge and PDOS. In Bader analysis, the electron charge distribution from the DFT calculation ($\Delta\rho_{FeCo/FeCoP} - \Delta\rho_{FeCo} - \Delta\rho_{FeCoP}$) was partitioned and assigned to individual atoms.

Three adsorbates are chosen, namely O, OH, OOH, which are known to be key intermediates in oxygen evolution reaction (OER). Reaction

$$no. of\ \ O_2 = (|j| \frac{mA}{cm^2})(\frac{1Cs^{-1}}{1000mA})(\frac{1mol\ \ e^-}{96485.3C})(\frac{1mol\ \ O_2}{4mol\ \ e^-})(\frac{6.022 \times 10^{23}\ \ O_2\ \ molecules}{1mol\ \ O_2}) = |j| * 1.5603 * 10^{15}\ \ \frac{O_2/s}{cm^2} per\ \frac{mA}{cm^2} \tag{4}$$

energies are calculated against H$_2$O(g) and H$_2$(g), using the computational hydrogen electrode (CHE) model.

$$E_{OH} = E_{surf+*OH} - E_{surf} - E_{H_2O} + \frac{1}{2}E_{H_2} \tag{8}$$

$$E_O = E_{surf+*O} - E_{surf} - E_{H_2O} + E_{H_2} \tag{9}$$

$$E_{OOH} = E_{surf+*OOH} - E_{surf} - 2E_{H_2O} + \frac{3}{2}E_{H_2} \tag{10}$$

To account for the Gibbs free energy difference between the reaction steps, the following equations as implemented by Rossemeisl et al. is used [57].

$$\Delta G_1 = E_{OH} + \Delta E_{ZPE} - T\Delta S - eU \tag{11}$$

$$\Delta G_2 = E_O - E_{OH} + \Delta E_{ZPE} - T\Delta S - eU \tag{12}$$

$$\Delta G_3 = E_{OOH} - E_O + \Delta E_{ZPE} - T\Delta S - eU \tag{13}$$

$$\Delta G_4 = 4.92 - E_{OH} + \Delta E_{ZPE} - T\Delta S - eU \tag{14}$$

where E_{ZPE} is the zero point energy correction, and U is the applied potential. Zero point energies and entropic corrections are taken from reference [58].

From the above equations, overpotential can be obtained by using the following relationship, and results of OER steps according to the potentials are shown in Fig. 4 and Table S6.

$$\eta^{OER} = \frac{|\max\{\Delta G_1, \Delta G_2, \Delta G_3, \Delta G_4\}|}{e} - 1.23V \tag{15}$$
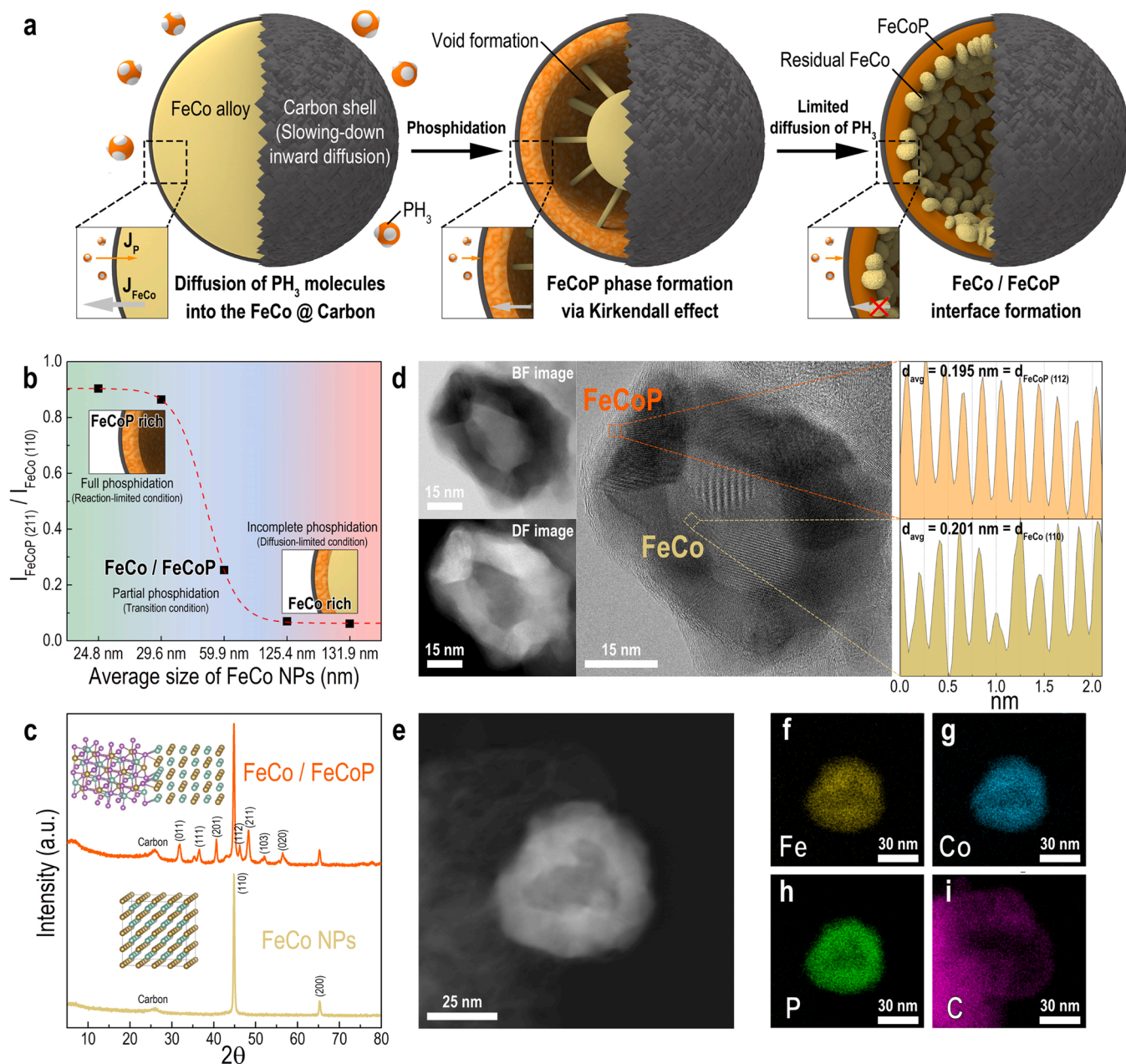
Fig. 1. (a) Schematic of the design of the heterointerface structure. (b) Degree of the phosphidation calculated from the ratio of X-ray diffractometry (XRD) intensities of FeCoP (211) and FeCo (110) with respect to the initial complexation ratio between TA and metal ions. (c) Comparative XRD patterns of the FeCo/FeCoP heterointerface structure and bare FeCo. (d) High resolution transmission electron microscopy (HR-TEM) results with bright-field (BF), dark-field (DF), and HR images of the heterointerface structure with corresponding *d*-spacing analysis. (e) High-angle annular dark-field (HAADF) image of the FeCo/FeCoP catalyst with the corresponding elemental mapping for Fe, Co, P, and C.

3. Results and discussion

3.1. Synthesis and characterisation of the FeCo/FeCoP/C heterointerface structure

To form the heterointerface structure, a graphitic carbon layer (GCL) was introduced to regulate the rate of the inward gas diffusion at the interface between the FeCo NPs and external carbon matrix. The permeate transport of the PH$_3$ gas molecules during phosphidation could be effectively regulated owing to the dense atomic arrangements in the GCL. Fig. 1a shows the schematic of the entire synthesis process employed for the fabrication of the heterointerface structure. First, the GCL-encapsulated FeCo alloy NPs embedded in an amorphous carbon matrix (FeCo/GCL/C, Fig. S1) were prepared through the hydrothermal treatment of the complex containing the phenolic ligand of tannic acid (TA) (Fig. S2) and alloy-constituting metal ions (Fe and Co), followed by thermal annealing, i.e., carbonization at 900 °C under inert conditions. According to our previous report, catalytic metal centers adjacent to the TA molecules could facilitate the simultaneous interlinking of the C–C coupling and C–O bonds [41]. As a result, a well-defined GCL forms after carbonization owing to the development of a highly planarized molecular configuration of the aromatic carbons. In this study, the introduction of the GCL diffusion barrier was accomplished through a single synthetic process, which is considerably simpler than the conventional processes that require additional coating over the colloidal NPs. To produce the FeCo/FeCoP/GCL/C heterointerface structure (denoted as FeCo/FeCoP), the GCL-encapsulated FeCo NPs were then subjected to a phosphidation reaction. As previously discussed, the GCL barrier surrounding the FeCo NPs severely limits the inward diffusion of PH$_3$ during phosphidation. Simultaneously, the outward diffusion of FeCo to the reaction interface was controlled by varying the size of the NPs. Moreover, TA molecules contain abundant intrinsic chelation sites, which allowed the wide range of variation in the complexation ratio between TA and chelated metal ions from 1:0.05–1:20. After carbonization, the size of the produced FeCo NPs varied from 20 to 140 nm as excess TAs and metal ions were used, respectively (Fig. S1a). Overall, the degree of FeCo phosphidation and thickness of the resulting FeCoP layer were effectively controlled.

To study the effect of particle size on the evolution of the FeCo/FeCoP heterointerface structure, XRD was performed on samples prepared after the phosphidation of FeCo NPs of varying particle sizes. The degree of phosphidation was estimated from the ratio of the crystallographic intensities of the FeCo (110) and FeCoP (211) planes (Fig. S1b). When relatively large FeCo NPs were used, the outward diffusion required for the formation of the FeCoP phase was limited, yielding an internal residual FeCo phase (Fig. 1b). In contrast, the entire FeCo phase was converted into FeCoP when small FeCo NPs were used despite the regulated inward diffusion of PH$_3$ through the GCL. Therefore, the incomplete phosphidation of the FeCo NPs with diameters > 120 nm can be attributed to the extended diffusion pathway in the large particles and to the retarded interdiffusion of FeCo in the newly formed FeCoP phase.

Typically, hollow core-laden structures are produced when the conventional approaches of KE application to NPs are employed [33–35]. In the commonly used methods, the inner species are promoted to diffuse outward while being provided with reacting species externally. In contrast, in the present study, the GCL surrounding the FeCo NPs inhibited the inward gas diffusion of the phosphorous anions. Consequently, a sluggish diffusion process drives the KE to operate under anion diffusion-limited conditions within the restricted volume of the FeCo phase. When the kinetics of the outward diffusion of FeCo is not compensated by that of the inward diffusion of PH$_3$ through the GCL, the phosphidation reaction occurs through a diffusion-limited regime. Accordingly, the partial phosphidation reaction forms the FeCo/FeCoP heterointerface. Herein, a FeCo/FeCoP heterointerface structure was

successfully synthesized using moderately sized FeCo NPs with an approximate diameter of 60 nm. To verify the function of GCL as a diffusion barrier, a control sample was produced after the phosphidation of similarly sized FeCo NPs without GCL (Fig. S3). XRD and TEM analyses confirmed that a single FeCoP phase with hollow internal cores was produced using the bare FeCo NPs, thereby proving the effectiveness of the GCL as a diffusion barrier. Therefore, the incorporation of GCL is necessary to induce the anion diffusion-limited KE for the creation of well-defined heterointerface structures.

When the size of the FeCo NPs was optimized to 60 nm, diffraction peaks corresponding to the FeCo alloy, FeCoP, and carbon phases were observed, confirming the successful formation of the FeCo/FeCoP/C heterointerface (FeCo: JCPDS no. 49–1567, FeP: JCPDS no. 01–078–1443, and CoP: JCPDS no. 00–029–0497) structure (Fig. 1c). Fig. 1d shows the results of the structural and morphological analyses of the heterointerface obtained through transmission electron microscopy. The presence of a graphitic carbon shell has also been confirmed by a magnified TEM image and its corresponding D-spacing analysis (Fig. S4). On one hand, the BF and DF TEM images of a single NP encased in a carbon matrix clearly depict the core phase and the surface layer with a unique covering. On the other hand, the HR-TEM image in Fig. 1d further confirmed the presence of an intact and isolated FeCo domain in the core region and a surface-enriched FeCoP phase with the corresponding D-space distributions of FeCo (110) and FeCoP (112), respectively. These results indicate the presence of a well-developed heterointerface structure. The scanning transmission electron microscopy (STEM) image (Fig. 1e) and corresponding energy dispersive spectroscopy (EDS) elemental maps (Fig. 1f and Fig. S5) show the distribution of Fe, Co, P, and C in the heterointerface structure. Therefore, a highly tunable heterointerface can be synthesized by employing diffusion-regulated KE through the incorporation of a GCL as the diffusion barrier.

3.2. Determination of the oxidation state of Fe at the interface

After the formation of the FeCo/FeCoP heterointerface through the proposed controlled phosphidation process, the undesirable lattice mismatch between the FeCo and FeCoP phases causes imbalanced valence states of the metals at the interfaces. Fig. 2 and Fig. S6 show the XANES spectra of the FeCo/FeCoP heterointerface structure, single phase FeCoP, single phase FeCo alloy, and reference materials (Fe$_2$O$_3$ and CoO) to comparatively investigate the oxidation state of the metal atoms in these samples. The shifting of the pre-edge position (Fe K-edge) of FeCo/FeCoP to a higher energy region (7124.3 eV) relative to that of the FeCoP edge position (7119.6 eV) indicates that the oxidation state of the Fe atoms is higher in the FeCo/FeCoP heterointerface than that in the single FeCoP phase (Fig. 2a). The accurate value of the oxidation state was determined by extrapolating the corresponding edge position in the XANES spectra (Fig. 2b). Significantly, the oxidation state of the Fe atoms in FeCo/FeCoP was higher (Fe$^{+3.18}$) than that of the Fe atoms in the single phase FeCoP (Fe$^{+1.98}$) and even in the reference Fe$_2$O$_3$ (Fe^{+3}). These results demonstrate that the oxidation state of the metal atoms in the bimetallic (phosphide) system can be substantially increased through the facile structural modification of the interface. In contrast, a similar effect on oxidation was achieved in previous reports through more difficult approaches, such as the external incorporation of high-valence metal atoms and intentional utilization of high-valence metal modulators [10]. The wavelet transform (WT) of k_3-weighted extended X-ray absorption fine structure (EXAFS) signals was performed to quantitatively compare the atomic distribution information with respect to the R-space (radial space) and k-space (energy space) and consequently gain a comprehensive understanding of the atoms surrounding the central atom. The WT of EXAFS signals is beneficial for distinguishing the different types of atoms within one atomic shell; the EXAFS signals of different atomic components cannot be effectively separated through the conventional Fourier transform (FT) approach.
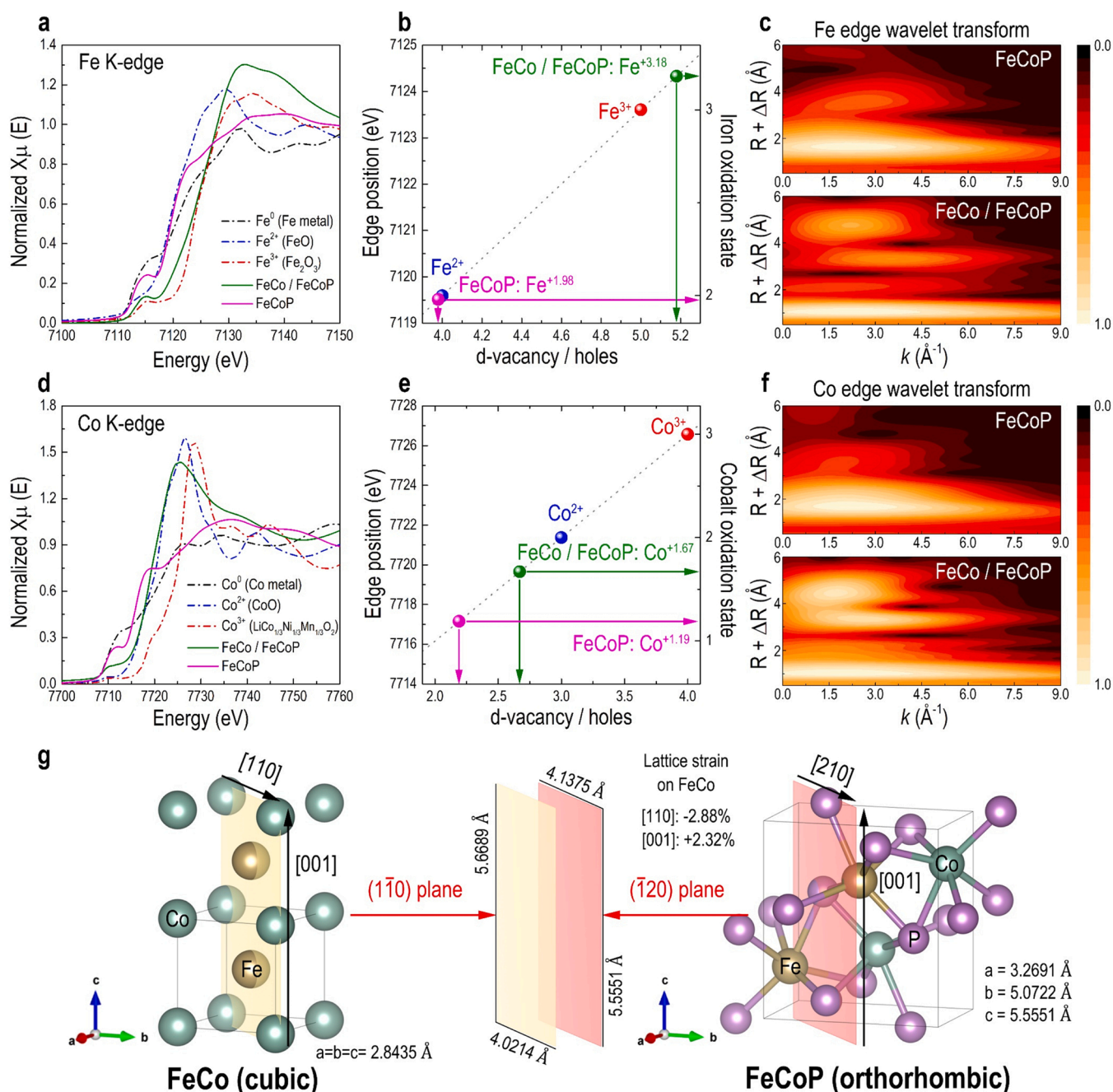
Fig. 2. Experimental XAS analyses of heterointerface-structured FeCo/FeCoP, single phase FeCoP, and reference materials. (a) Normalised Fe K-edge XANES spectra. (b) Plot of the integrated edge position versus d-band vacancy and Fe oxidation state. (c) WT of the k_3-weighted Fe K-edge EXAFS signals. (d) Normalised Co K-edge XANES spectra. (e) Plot of the integrated edge position versus d-band vacancy and Co oxidation state. (f) WT of the k_3-weighted Co K-edge EXAFS signals. (g) Schematic of interface formation on cubic FeCo and orthorhombic FeCoP lattices.

After WT, similar intensity profiles were obtained for the FeCo/FeCoP and FeCoP samples near 1.0 Å. However, differences in the total intensity profiles of the two were apparent (Fig. 2c and Fig. S7). Moreover, the WT intensity profile of FeCo/FeCoP did not match those of the single FeCo phase and metallic Fe (Fig. S7). These results clearly suggest that the high oxidation state of Fe originated from the heterointerface of FeCo/FeCoP. As expected, inherent Fe oxidation was also observed on the FeCoP and FeCo phases.

Fig. 2d and e show the analysis of the Co K-edge of the XANES spectra of FeCoP and FeCo/FeCoP. At the pre-edge region, the FeCo/FeCoP edge position was observed at a higher energy (7718.9 eV) relative to that of the FeCoP edge position (7716.2 eV). This implies that the oxidation state of the Co atoms in the FeCo/FeCoP sample is also higher than that of the Co atoms in FeCo (Fig. 2d). From the quantitative analysis of the XANES of the Co K-edge (Fig. 2e), the oxidation state of the Co atoms in FeCo/FeCoP ($Co^{+1.67}$) was distinct in comparison to that of the Co atoms present in the single phase FeCoP ($Co^{+1.19}$) sample; moreover, the Co atoms in the CoO reference material exhibited a higher oxidation state (Co^{+2}). In comparison, the observed increase in the oxidation state of the Co atoms (1.19–1.67) on the single FeCoP phase and FeCo/FeCoP heterointerface was not comparable with that of the Fe atoms (1.98–3.18). Therefore, the heterointerface structuring of the catalyst predominantly modified the valency of the Fe atoms. This finding agrees well with those observed for some previously reported Fe-containing $Ni(Fe)O_xH_y$ or Co

(Fe)O$_x$H$_y$ catalysts in which Fe atoms exhibited a higher oxidation state than other metal atoms [4,5,9]. The WT intensity of the Co K-edge XANES spectrum of FeCo/FeCoP was distinguishable from those of the Co atoms in the Co metal, FeCo alloy, and single FeCoP phase. Therefore, the increase in the oxidation state of the Co atoms can also be attributed to the formation of the FeCo/FeCoP heterointerface.

Considering the XRD and X-ray absorption spectroscopy (XAS) results for the representative FeCo/FeCoP heterointerface structure, the model structure was designed using cubic FeCo and orthorhombic FeCoP lattices (Fig. 2g). The interface was constructed using the FeCo $(1\bar{1}0)$ and FeCoP $(\bar{1}20)$ planes, which are depicted in yellow and orange, respectively. The $(1\bar{1}0)$ plane of FeCo was specified by two individual orthogonal vectors, namely, FeCo [110] (4.0214 Å) and FeCo [001] (2.8435 Å). Similarly, the $(\bar{1}20)$ plane of FeCoP was defined using the [210] and [001] vectors, which are perpendicular to each other, with corresponding lengths of 4.1375 and 5.5551 Å, respectively. The length of FeCo [110] (4.0214 Å) was approximately similar to that of FeCoP [210] (4.1375 Å) with an imprecision of –2.88%. When the length of FeCo [001] was doubled (2 × 2.8435 =5.6870 Å), the length of FeCo [001] was nearly aligned with that of FeCoP [001] (5.5551 Å) with a mismatch of 2.32%. This as-defined plane junction is possibly the most probable structure; the other probable plane junctions exhibited a highly strained lattice plane mismatching of more than 5%. Therefore, the FeCo/FeCoP heterointerface was modelled by aligning the $(1\bar{1}0)$ plane of FeCo and the $(\bar{1}20)$ plane of FeCoP with the feasible strain ranges of FeCo [110] and [001] by –2.88% and 2.32%, respectively.

3.3. Theoretical analysis of the high oxidation state of the Fe centres at the FeCo/FeCoP interface

To gain a comprehensive understanding of the experimentally observed FeCo/FeCoP interface in Figs. 1 and 2, DFT calculations were performed to validate the formation energies of the heterointerface. An energetically optimized model interface structure was created for the FeCo/FeCoP heterointerface (Fig. 2g and 3a) using the FeCo $(1\bar{1}0)$ and FeCoP $(\bar{1}20)$ planes. Among the four interface models that depend on the termination of the repeating units in each phase, the most energetically stable FeCo/FeCoP interface was chosen for further theoretical

calculations (Fig. S8 and Table S1). The formation energetics of FeCo/FeCoP were also studied through DFT calculations to quantify the spontaneity of heterointerface formation using the 1-interface model [59]. The calculated interface energy was negative (–473.7 meV Å^{-2}), indicating that the FeCo/FeCoP heterointerface readily forms through a diffusion-regulated phosphidation process (Fig. S9). Therefore, the results of the DFT calculations support the formation of the heterointerface previously proven by experimental material characterizations.

In the model structure in Fig. 3a and Fig. S10, the Fe and Co atoms were connected by P atoms at the interface. To fully explain the origin of the unbalanced valence states of the metals at the interface, the oxidation states of the metal centers were computed and labelled accordingly based on the atomic positions assigned to the model interface structure (Fig. 3a and Fig. S10). Compared with the typical oxidation states of Fe and Co centers in a bare FeCoP lattice, the oxidation states of the Fe (Fe **13**, Fe$^{+3.156}$) and Co (Co **18**, Co$^{+3.137}$) atoms were higher than those of the neighboring Fe and Co atoms. The phosphorus-deficient covalent bonds of Fe and Co centers near the interface (Fe **13, 17**, and Co **13, 18**) possibly induced unusual cation coordination environments (e.g., 4-coordinated bisphenoidal or 5-coordinated square pyramidal) instead of the conventional 6-coordinated octahedral geometry. This result, along with the experimental XAS observations, reveals that high oxidation states of metal atoms can be achieved through the formation of a heterointerface.

To study the interfacial electron transfer processes, Bader charge analysis was performed (Fig. 3b and c). To effectively visualize the charge transfer between the FeCo and FeCoP phases, the planar average charge density was plotted normal to the heterointerface junction along the z-direction. Charge accumulation was strongly facilitated at the Fe and Co centers of the FeCoP phase near the interface (Fig. 3b), which is indicative of the charge transfer processes between the FeCo and FeCoP phases. Moreover, the 2D charge density profiles at the sections sliced at I and II (pink regions in Fig. 3a and b) illustrate the charge transfer details at the regions containing Fe (Fe **13**) metal centers with a high oxidation state (Fig. 3c). This confirms that extensive charge transfer occurs at the interface, which agrees well with the trend depicted in Fig. 3b. Overall, the metal center with a high oxidation state at the interface possesses low intrinsic electron density; therefore, the electron-rich metallic-bonded alloy of the FeCo phase serves as a charge
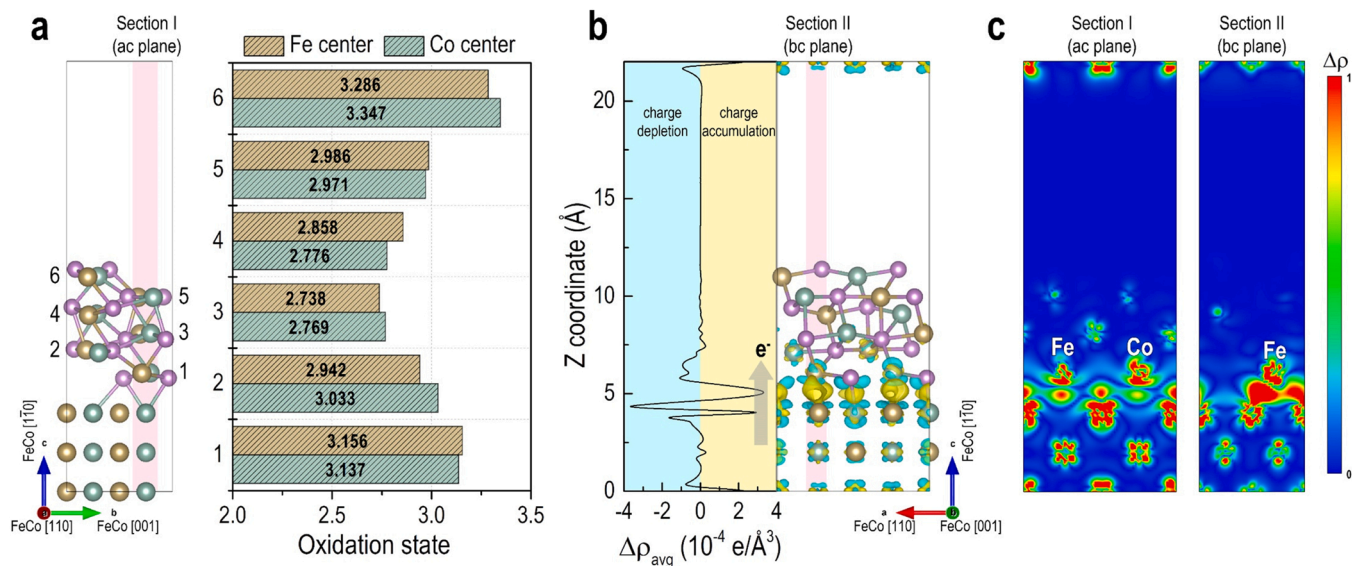

Fig. 3. DFT calculations to understand the oxidation state and charge transfer properties at the interface. (a) (left) Relaxed structure of the FeCo/FeCoP interface formed between cubic FeCo and orthorhombic FeCoP. (right) Computed oxidation state of the metal centre in the FeCo/FeCoP structure (1st to 6th layer of FeCoP). (b) Planar averaged-charge density difference ($\Delta\rho_{avg}$) with respect to the Z-coordinate for the FeCo/FeCoP structure. Charge density difference caused by the formation of interface is displayed on the right, where yellow and pale blue-shaded regions represent charge accumulation and depletion, respectively. (c) Electronic charge density profile of FeCo/FeCoP sliced at sections I and II.

reservoir and delivers charge to electron-deficient atoms in a substantial manner. This oxidation state–electron transfer relationship at the interface could be further correlated to other physicochemical properties of the local interface, such as electrocatalytic activity, in which the transfer of electrons is critical to the adsorbate–surface interaction.

3.4. OER performance of the FeCo/FeCoP heterointerface structure

The high oxidation state of the metal atoms (Figs. 2 and 3) can improve the OER activity of the FeCo/FeCoP interface structure [4,5,9]. To investigate the structure–activity relationship, electrocatalytic water oxidation experiments were conducted. Particularly, the OER performance of the designed electrocatalysts was evaluated in 1.0 M KOH electrolyte using a standard three-electrode system (Fig. 4a). Fig. 4a
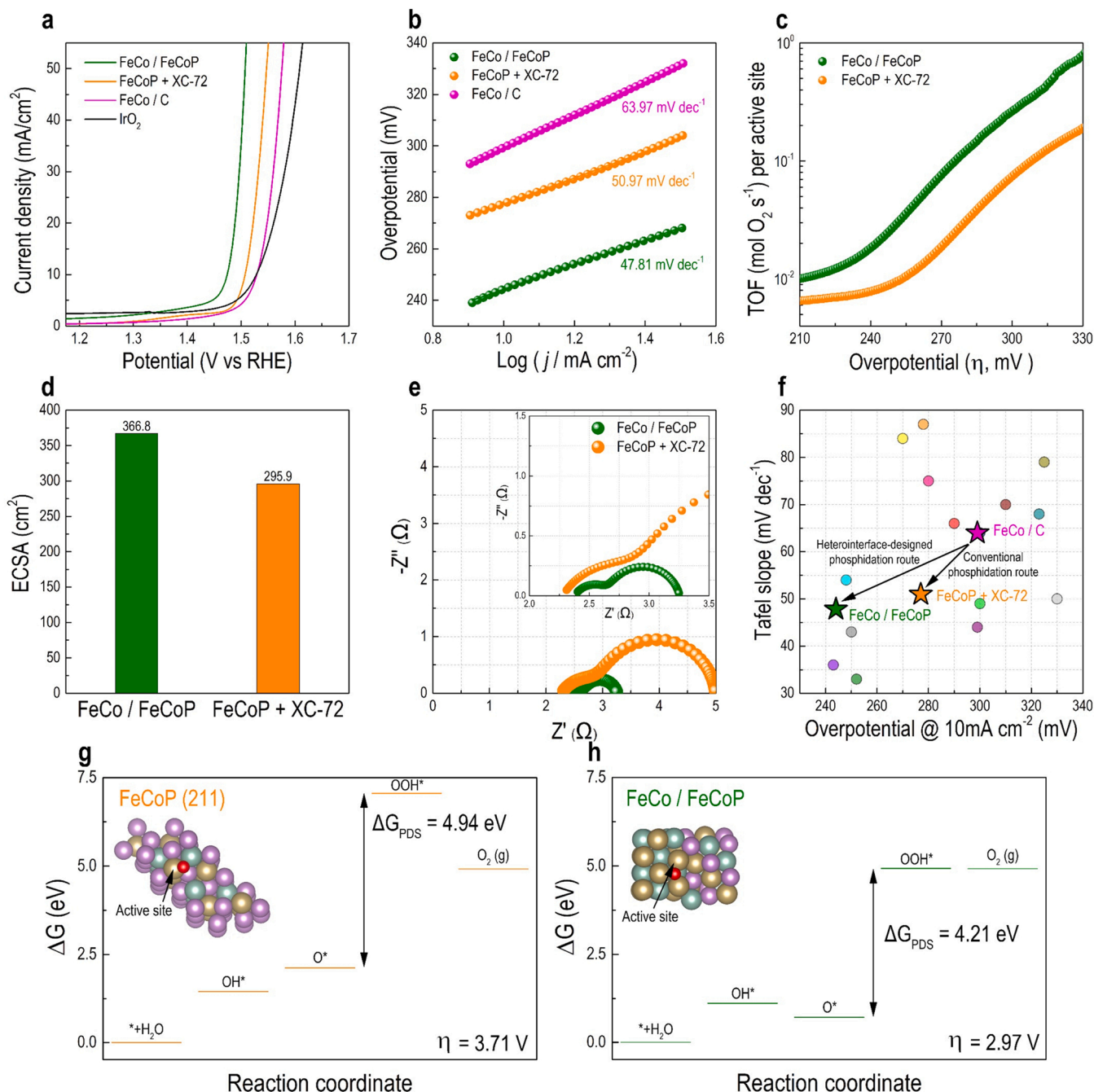
Fig. 4. . (a) *iR*-compensated LSV graphs of the different electrocatalysts recorded in a 1.0 M KOH electrolyte. (b) Corresponding Tafel plots. (c) Comparison of the TOF of the different electrocatalysts. (d) Electrochemically active surface area (ECSA) of the electrocatalysts calculated using double layer capacitance measurements. (e) Nyquist plots for various electrocatalysts measured through electrochemical impedance spectroscopy (EIS) at 1.574 V vs. RHE from 0.01 Hz to 100 kHz; 2TS model was used to fit the corresponding impedance spectra. (f) Figure of merit of the OER performance with respect to activity (overpotential at 10 mA cm^{-2}) and kinetics (Tafel slope) of the electrocatalysts presented in this study and some previously reported high-performance OER electrocatalysts (measured under alkaline electrolyte conditions, see details in Table S8). (g,h) DFT calculations for the explanation of the observed OER activity trend on the different electrocatalysts. (g) Gibbs free energy (ΔG) profile of the OER on the single FeCoP (211) planes, and (h) FeCo/FeCoP heterointerface-structured catalysts. Insets show the optimised structure of each catalytic site for the OER intermediates (brown: iron, blue: cobalt, purple: phosphorus, and red: oxygen).

shows the *iR*-compensated linear sweep voltammetry (LSV) graphs of the designed FeCo/FeCoP electrocatalysts, a commercial benchmark IrO$_2$ catalyst, and a control sample (physical mixture of FeCoP and Vulcan carbon (XC-72) and FeCo/C as a phosphidation precursor of FeCo/FeCoP). To ensure that the number of active sites is consistent among the samples, the weight ratio of the active catalyst (single phase FeCoP and FeCo) and carbon support (XC-72 Vulcan carbon) was fixed at 35:65, which corresponds to the amount of carbon in the FeCo/FeCoP sample confirmed through thermogravimetric analysis (TGA), X-ray photoelectron spectroscopy (XPS), inductively coupled plasma optical emission spectroscopy (ICP-OES), and TEM-EDS measurements (Fig. S11 and Table S2). Fig. S12 shows the overpotential of the electrocatalysts at a geometrical current density of 10 mA cm^{-2}. The OER activity of the FeCo/FeCoP heterointerface (η_{OER} = 244 mV) is better than those of FeCoP+XC-72 (η_{OER} = 277 mV), FeCo/C (η_{OER} = 299 mV), and IrO$_2$ (η_{OER} = 298 mV). The better OER activity of FeCo/FeCoP in comparison to those of FeCo and FeCoP can be attributed to its unique heterointerface structural features. Although a conventional phosphidation process could also improve the OER activity of the metallic FeCoP by transforming it to FeCoP, the observed activity enhancement of the FeCo/FeCoP heterointerface structure also motivates the development of novel synthesis strategies for highly active OER catalysts.

The Tafel plots in Fig. 4b, which reflect the kinetics of OER on the electrocatalyst surface, reveal that the lowest Tafel slope was recorded on the FeCo/FeCoP catalyst (47.81 mV dec^{-1}). The better OER kinetics observed on the heterointerface strongly suggests the existence of more energetically favorable active sites on FeCo/FeCoP for the adsorption/desorption of the reaction intermediates. The turnover frequency (TOF), which is one of the most important figures of merit for the evaluation of the inherent activity of an OER electrocatalyst, is calculated considering the number of the evolved O$_2$ molecules per second per active site [46–51]. The intrinsic OER performance of the FeCo/FeCoP catalyst increased by 3.5 times compared to that of the FeCoP+XC-72 sample; the calculated TOF at η_{OER} = 300 mV were 0.263 and 0.074 s^{-1}, respectively. The better intrinsic activity of FeCo/FeCoP than that of FeCoP+XC-72 possibly originated from the unique valence state of the metal sites at the interface of the electrocatalyst. The observed OER activity enhancement on FeCo/FeCoP can be correlated to the oxidation states of the metal sites in the catalyst. As previously discussed in Section 2.2, the oxidation state of the Fe atoms in FeCo/FeCoP (Fe$^{+3.18}$) was higher than that of the Fe species in bare FeCoP (Fe$^{+1.98}$). This potentially illustrated the structure–oxidation state–activity correlation. The FeCo/FeCoP interface structure containing high-valent Fe sites is presumed to be the key active site that activates the neighboring Co atoms, which consequently improves the OER performance collectively.

To evaluate the merits of the FeCo/FeCoP interface structure on other electrochemical characteristics, such as double layer capacitance and charge transfer resistance at the electrode/electrolyte interface, ECSA and EIS analyses were performed (Fig. 4d and e). On one hand, the significantly higher value of the ECSA of FeCo/FeCoP (366.8 cm^2) than that of FeCoP+XC-72 (295.9 cm^2) indicates that the heterointerface structure exhibited better electrochemical accessibility that potentially promoted more oxygen evolution per unit area. The high ECSA of the FeCo/FeCoP interface structure also confirms the presence of abundant high-valent Fe active sites, which drove more O$_2$ conversion (Fig. S13). On the other hand, the values of the solution resistance (R$_s$), interfacial layer resistance (R$_{sf}$) and charge-transfer resistance (R$_{ct}$) were determined from the Nyquist plots fitted using the 2TS model [60,61] (derived from the EIS spectra measured under identical OER experimental conditions, Fig. S14 and Table S3) as shown in Fig. 4e. The lower value of the R$_{ct}$ of FeCo/FeCoP (0.58 Ω) relative to that of FeCoP+XC-72 (1.97 Ω), which implies the robust charge transport property of FeCo/FeCoP, can be attributed primarily to the collective structural features of the interface containing high-valent Fe sites. The uniformly distributed active sites in the FeCo/FeCoP catalyst contribute to a lower value of R$_{sf}$ associated with electrolyte mass transport (0.29 Ω), in

contrast to that of FeCoP+XC-72 (0.75 Ω). The resulting performances are summarized in Fig. 4f, which clearly show that FeCo/FeCoP heterointerface catalyst exhibited considerably lower overpotential and higher TOF (Table S5). Therefore, FeCo/FeCoP exhibits more potential as a highly efficient active material for the OER in an alkaline medium compared to several previously reported metallic phosphide systems, such as FeCoP/CNT or FeCoP on Ni foam.

To understand the theoretical OER activities of the electrocatalysts, the changes in the Gibbs free energies of the four fundamental OER steps were calculated using DFT. The possible configurations of each adsorbate on the FeCo/FeCoP and FeCoP(211) surfaces were examined. Tables S6–S8 summarize the details of the adsorption (binding) energies, Gibbs free energies, and parameters used in each case. Herein, the overpotential (η) is considered as the difference between the practical (maximum ΔG at the rate-determining step (RDS)) and theoretical potentials for water splitting (1.23 V vs. SHE). Fig. 4g and h show the calculated values of the ΔG for each reaction step on FeCoP (211) and heterointerface-structured FeCo/FeCoP. The theoretical results reveal that FeCoP yield a relatively large value of η (3.71 V). For such cases, the RDS was the adsorption of the OOH* intermediate owing to the considerably strong binding between the surface Fe/Co atoms and the O* intermediate (Fig. S16).

At the FeCo/FeCoP interface, the binding energy of OOH* was considerably optimized possibly owing to the high oxidation state of the metal center at the interface. The theoretical results reveal that FeCo/FeCoP is a better OER electrocatalyst with a theoretical η of 2.97 V, which corresponds well with the results of the experimental electrochemical tests (Fig. 4a). The synergism between the FeCo and FeCoP phases at the interface was advantageous for the OER process. Considering the Gibbs free energy diagrams in Fig. 4h, the Fe^{+3} and Co^{+3} cations in FeCoP and metallic Fe^0 and Co^0 species in FeCo possess very weak and very strong adsorption for the OER, respectively. The spontaneous adsorption of the OER intermediates at the interface between FeCo and FeCoP can substantially optimize their Gibbs free energies, which significantly improves the OER performance of the catalyst, as evidenced by the theoretically optimized atomic structures shown in Fig. 3a. Therefore, in addition to the experimental electrochemical studies, the results of the DFT calculations further confirm the high OER performance of the FeCo/FeCoP interface.

Metal phosphide catalysts often undergo surface reconstruction due to oxidation at their surfaces, resulting in the transformation of metal phosphide into metal (oxy)hydroxide or oxide phases. Therefore, it is crucial to define the model catalyst surface and corresponding active sites when conducting density functional theory (DFT) calculations, taking into account surface reconstruction. In this context, previous studies on OER metal phosphide catalysts (Table S9) suggest that the original metal phosphide itself could be used as a precatalyst, whereas heterointerfaces with metal (oxy)hydroxide-reconstructed catalysts could be primarily utilized as a defined catalyst surface for DFT calculations. While our primary focus has been on modeling the active sites at the interface of the FeCo/FeCoP precatalyst, it is essential that future studies include comprehensive DFT analyses that take surface reconstruction into account.

3.5. AEM electrolyser performance catalysed by FeCo/FeCoP anode

MEA-based water electrolysers have been extensively used for practical H$_2$ fuel production [42,62,63]. To investigate the commercial viability of the catalyst under practical operating conditions in a MEA-scale device, the activity of the FeCo/FeCoP in an AEMWE was evaluated (Fig. 5a). Herein, FeCo/FeCoP and commercial PtRu/C were used as anode and cathode, respectively. The anion exchange membrane used was the ammonium-functionalized polynorbornene (Fig. S17) [43]. Water splitting was performed at 80 °C using a 1.0 M KOH circulating electrolyte (Fig. 5b). For comparison, an AEMWE using a FeCoP+XC-72-based anode was fabricated and tested under identical
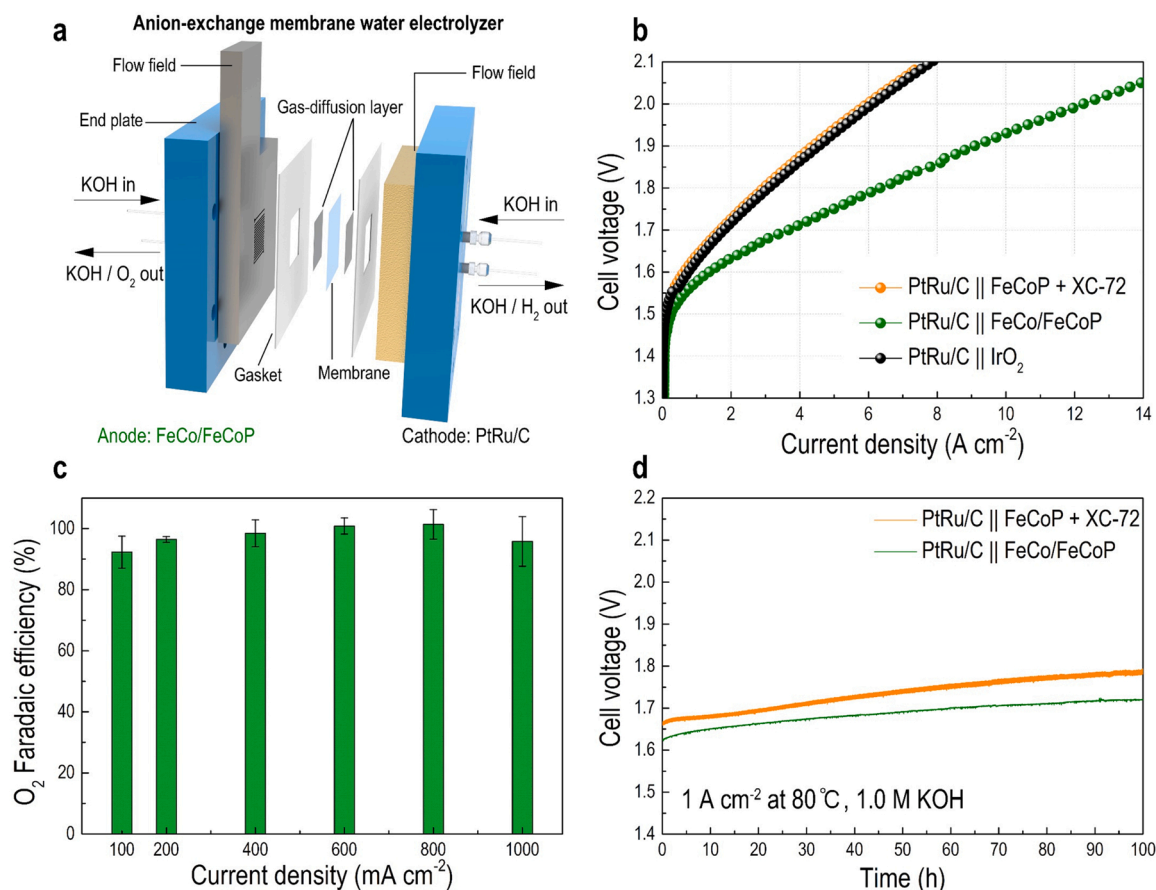
Fig. 5. (a) Schematic illustration of AEMWE device. (b,c) AEM electrolyser performance of cells catalysed using different anodes (without *iR*-correction). (b) Performance of the membrane electrode assemblies (MEAs) employing FeCo/FeCoP and FeCoP+XC-72 electrodes at the anode. In both cases, ammonium-functionalized polynorbornene and PtRu/C were used as the AEM and the catalysts on the cathode, respectively. AEM water electrolysis was performed under ambient pressure conditions at 80 °C with KOH solutions flowing in both the anode and cathode. (c) Oxygen Faradaic efficiency of FeCo/FeCoP under constant current densities ranging from 100 mA cm^{-2} to 1000 mA cm^{-2}. (d) Stability of the MEAs with FeCo/FeCoP and FeCoP+XC-72 electrocatalysts at 80 °C at a constant current density of 1 A cm^{-2}.

conditions. The current density of the MEA with the FeCo/FeCoP electrode at 2.0 V was 12.26 A cm^{-2} (green), which is higher than those recorded using IrO$_2$ (6.17 A cm^{-2}, black) and FeCoP+XC-72 (6.05 A cm^{-2}, orange) at the same cell potential. The cell voltage required for an industrially viable current output over 1 A cm^{-2} is only 1.58 V. Therefore, the heterointerface-structured FeCo/FeCoP catalyst also functions well under practical MEA cell operation conditions.

It should be noted that the superior MEA performance achieved in this study is a result of the synergistic effects of highly active FeCo/FeCoP catalyst, as well as other system configurations, including cathode catalyst, ionomers, and membranes. To comprehensively compare this MEA performance, a detailed system configuration and its corresponding performance are thoroughly presented and compared in Table S10. Furthermore, it is noteworthy to mention that the oxygen Faradaic efficiency (FE) of FeCo/FeCoP catalysts acquired from MEA-based water electrolyser was found to be in the range of 95–105% (as depicted in Fig. 5c), which strongly suggests that the electrocatalytic process in this system is mainly governed by the OER, and there were no other competing side reactions such as the corrosion effect. These results signify that the synthesis approach adopted in this study has the potential to produce electrocatalysts that are both exceptionally efficient and long-lasting in facilitating the production of clean fuels through water electrolysis. A long-term durability test was also performed on the FeCo/FeCoP electrode through the application of a constant current density of 1 A cm^{-2} for 100 h (Fig. 5d). The cell voltage of the MEA cell was retained even after 100 h of the stability testing. The degradation

rate was as low as 0.94 mV h^{-1}. Major voltage changes and serious performance degradation were not observed even under such harsh operating conditions. This result indicates that our designed FeCo/FeCoP electrocatalyst is also effective for application in such MEA-scale devices by demonstrating structure-performance relationships.

3.6. Post-analysis of FeCo/FeCoP catalyst

The surface reconstruction of an OER catalyst during water oxidation is a typical phenomenon that occurs, leading to changes in the catalyst's structure and behavior. To investigate this phenomenon, post-analysis of a FeCo/FeCoP sample was attempted after stability testing with a MEA configuration. The XRD patterns of post-samples, including FeCo/FeCoP, FeCoP + XC-72, and FeCoP samples, were compared, as shown in Fig. 6a. The results revealed that FeCoP + XC-72 and FeCoP samples exhibited a major phase change to FeCoOOH and CoFe$_2$O$_4$, with the FeP phase remaining. However, in the case of FeCo/FeCoP, its XRD pattern was different, including various preserved FeP and CoP phases. Thus, in FeCo/FeCoP, catalyst oxidation and surface reconstruction also occurred, but it showed different reconstruction behavior compared to typical FeCoP samples. TEM-EDS analysis, as shown in Fig. 6b – g, confirmed the above findings. The phosphorus signal was still detected in the core part of the catalyst with iron and cobalt signals, and the outermost phosphorous signal was leached, with the oxygen signal being dominantly detected. In the XPS analysis (Fig. S18), the phosphorus signal disappeared, presumably due to the leaching of outermost
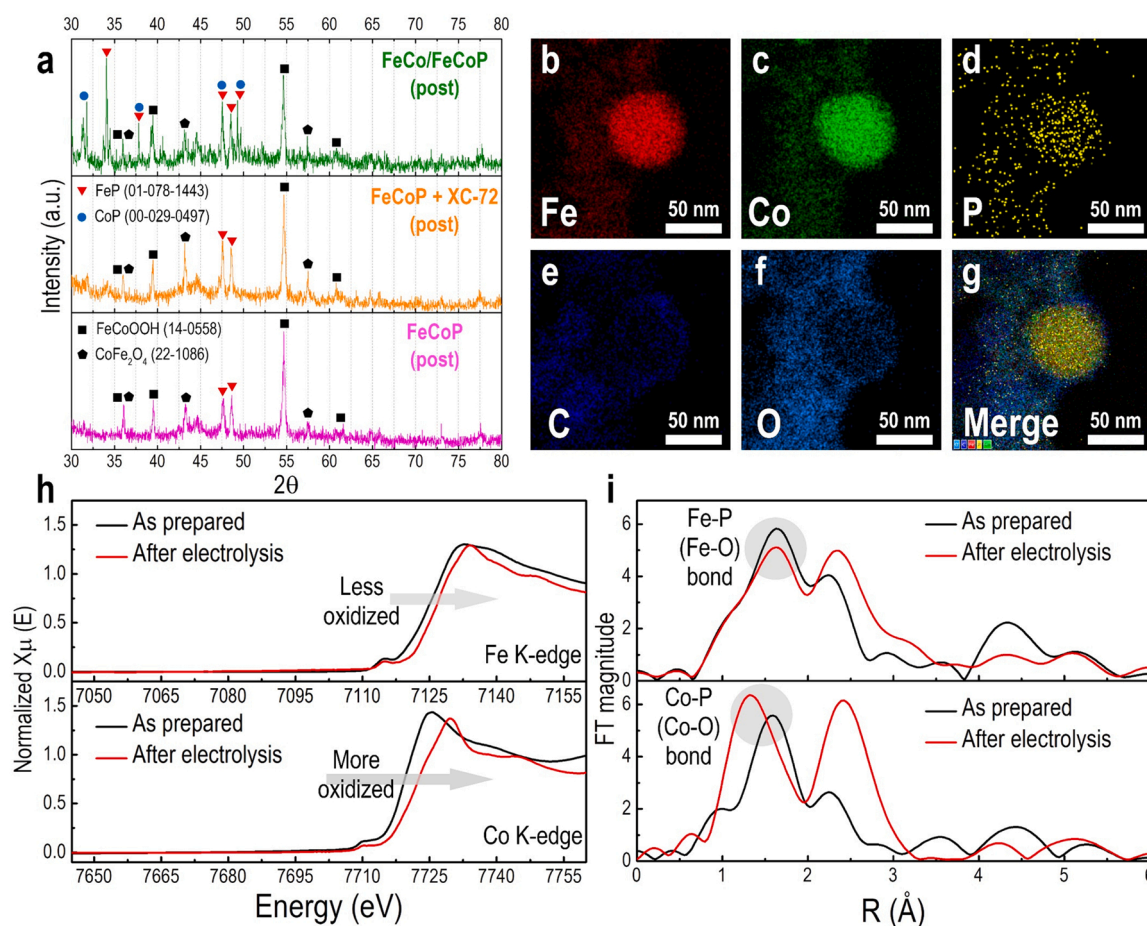
Fig. 6. Post-characterization results of FeCo/FeCoP catalyst. (a) Comparative XRD patterns of post samples, including FeCo/FeCoP, FeCoP+XC-72, and FeCoP. Post-FeCo/FeCoP sample shows distinct phase patterns compared to post-FeCoP sample. (b-g) Elemental mapping derived from the TEM-EDS analysis, including signals of (b) Fe, (c) Co, (d) P, (e) C, (f) O, and (g) a merged image. (h,i) Post-XAS analysis of FeCo/FeCoP after electrolysis. (h) Comparative normalized XANES spectra, including Fe K-edge (upper) and Co K-edge (lower), respectively. (i) Comparative normalized EXAFS spectra, including Fe K-edge (upper) and Co K-edge (lower), respectively. Fe oxidizes to a lesser extent than Co, with no noticeable shift in Fe-P (Fe-O) bond length.

elements, as well as the limited measurement depth of XPS. Compared to FeCo/FeCoP, bare FeCoP showed complete morphological change in TEM analysis, as detected in XRD (Fig. 6a and Fig. S19). Lastly, ICP-OES analysis was conducted to detect any catalyst-leached elements in the electrolyte (Fig. S20). The electrolyte solution was examined after the OER test to compare the levels of phosphorus in each catalyst. The FeCo/FeCoP catalyst was compared to bare FeCoP, and the results showed that the electrolyte containing the FeCo/FeCoP electrode contained 1.58 ppm of phosphorus, while the bare FeCoP contained 6.03 ppm, which is four times higher than that of the FeCo/FeCoP catalyst. Overall, our findings suggest that the FeCo/FeCoP catalyst with its carbon shell may play an effective role in preventing the leaching of phosphorus. This implies that the graphitic carbon shell surrounding the FeCo/FeCoP catalyst may mitigate severe oxidation reactions.

Post-XAS analysis was performed on the FeCo/FeCoP catalyst to investigate any structural changes, oxidation states, and bonding information at each metal edge (Fig. 6h and i). Due to the oxidation effect, the XANES analysis exhibited an obvious increase in the oxidation state, suggesting the formation of Fe/Co (oxy)hydroxide phases (Fig. 6h). The EXAFS analysis revealed distinct trends at the Co and Fe edges (Fig. 6i). At the Co edge, there was a notable contraction in bonding and a shift in peak occurrence in the 1–2 Å range, which is indicative of the formation of Co-O bonds. In contrast, the Fe edge analysis revealed that the Co-P (or Co-O) bonds had nearly the same bonding length, highlighting the intact nature of the Fe edge sites even after the OER test. In addition, we conducted a post-comparison experiment to indirectly discuss the active

sites of FeCo/FeCoP sample (Fig. S21). Compared to the OER performance of Fe/Co (oxy)hydroxide phases derived from typical FeCoP phases, the OER performance of post-catalysts of FeCo/FeCoP, including a mixed phase of Fe/Co phosphide and Fe/Co oxide, was superior, providing basis that the catalyst containing a metal (Fe) phosphide interface likely serves as the active site. Furthermore, FeCo/FeCoP exhibited a marginal decrease in activity, while FeCoP displayed a considerable difference in activity between the pre- and post-samples.

4. Conclusions

In summary, the significant OER activity of a heterointerface-structured FeCo/FeCoP catalyst was demonstrated by inducing the formation of high-valent Fe atoms at the interface. Utilising a GCL as a diffusion barrier, the diffusion-controlled phosphidation of FeCo/C NPs induced the KE, which consequently formed the FeCo/FeCoP heterointerface. Systematic structural and morphological characterisations through XRD and HR-TEM analyses revealed the successful formation of the FeCo/FeCoP heterointerface. Comparative XAS and DFT analyses confirmed that the oxidation state of Fe in the synthesised FeCo/FeCoP heterointerface ($Fe^{+3.18}$) was considerably higher than that of the Fe atoms ($Fe^{+1.98}$) in the parent materials. The OER activity of the heterointerface-structured FeCo/FeCoP catalyst was substantially better than those of the single phase FeCo or FeCoP catalysts. In a 1.0 M KOH electrolyte, the recorded overpotential at 10 mA cm^{-2} and Tafel slope on FeCo/FeCoP were 244 mV and 47.8 mV dec^{-1}, respectively. The

relatively high TOF of the FeCo/FeCoP electrocatalyst (0.263 s^{-1} at an overpotential of 300 mV) indicates that the high activity at the FeCo/FeCoP interface possibly originated from the high-valent active sites. AEMWE was performed to evaluate the practical viability of catalysts. At a cell voltage of 2.0 V, the current density attained using the FeCo/FeCoP electrode at 80 ℃ under a flow of 1.0 M KOH was as high as 12.26 A cm^{-2}. Using a heterointerface model structure constructed through theoretical calculations, the high activity of the high-valent Fe active sites at the FeCo/FeCoP interface was confirmed. The adsorption energetics at the high-valent Fe sites in the FeCo/FeCoP interface obtained through DFT calculations corresponded well with experimentally calculated low overpotential of the catalyst, confirming further that the good OER activity of the catalyst was caused by the high oxidation state of Fe and that the high-valent Fe atoms were primarily the active sites. Therefore, the design of a sophisticated FeCo/FeCoP interface with a distinct oxidation state presented herein offers a comprehensive understanding on the structure–oxidation state–OER activity relationship. Furthermore, the results of this study will facilitate the development of novel strategies for developing materials for next-generation energy conversion systems.

CRediT authorship contribution statement

Gwan Hyun Choi: conceived the idea, conducted the experiments, analyzed the data, performed DFT studies using QUANTUM ESPRESSO, conducted AEMWE performance measurement and wrote the manuscript. **N. Clament Sagaya Selvam:** conceived the idea, conducted the experiments, analyzed the data, and wrote the manuscript. **Hyunwoo Kim:** performed the XAFS measurement and post analysis. **Young Sang Park:** conducted the AEMWE performance measurement. **Jiyoon Jung:** synthesized TMA-70 and AEMs for AEMWE measurement. **Myeong Gyun Nam:** provided major assistance. **Hyo Sang Jeon:** Faradaic efficiency measurement and XAFS data discussion. **Albert Sungsoo Lee:** supervised the research. **Won-Sub Yoon:** supervised the research. **Pil Jin Yoo:** supervised the research.

Declaration of Competing Interest

The authors declare that they have no known competing financial interests or personal relationships that could have appeared to influence the work reported in this paper.

Data Availability

Data will be made available on request.

Acknowledgements

Appendix A. Supporting information

Supplementary data associated with this article can be found in the online version at doi:10.1016/j.apcatb.2023.122816.

References

[1] J. Song, C. Wei, Z.-F. Huang, C. Liu, L. Zeng, X. Wang, Z.J. Xu, A review on fundamentals for designing oxygen electrocatalysts, Chem. Soc. Rev. 49 (2020) 2196–2214.

[2] H.N. Nong, L.J. Falling, A. Bergmann, M. Klingenhof, H.P. Tran, C. Spöri, R. Mom, J. Timoshenko, G. Zichittella, A. Knop-Gericke, S. Piccinin, J. Pérez-Ramírez, B. R. Cuenya, R. Schlögl, P. Strasser, D. Teschner, T.E. Jones, Key role of chemistry versus bias in electrocatalytic oxygen evolution, Nature 587 (2020) 408–413.

[3] J. Liu, H. Liu, H. Chen, X. Du, B. Zhang, Z. Hong, S. Sun, W. Wang, Progress and challenges toward the rational design of oxygen electrocatalysts based on a descriptor approach, Adv. Sci. 7 (2020) 1901614.

[4] L.J. Enman, M.B. Stevens, M.H. Dahan, M.R. Nellist, M.C. Toroker, S.W. Boettcher, Operando x-ray absorption spectroscopy shows iron oxidation is concurrent with oxygen evolution in cobalt–iron (oxy) hydroxide electrocatalysts, Angew. Chem. Int. Ed. 57 (2018) 12840–12844.

[5] M.B. Stevens, C.D. Trang, L.J. Enman, J. Deng, S.W. Boettcher, Reactive Fe-sites in Ni/Fe (oxy) hydroxide are responsible for exceptional oxygen electrocatalysis activity, J. Am. Chem. Soc. 139 (2017) 11361–11364.

[6] J.Y. Chen, L. Dang, H. Liang, W. Bi, J.B. Gerken, S. Jin, E.E. Alp, S.S. Stahl, Operando analysis of NiFe and Fe oxyhydroxide electrocatalysts for water oxidation: detection of Fe^{4+} by Mossbauer spectroscopy, J. Am. Chem. Soc. 137 (2015) 15090–15093.

[7] D. Friebel, M.W. Louie, M. Bajdich, K.E. Sanwald, Y. Cai, A.M. Wise, M.-J. Cheng, D. Sokaras, T.-C. Weng, R. Alonso-Mori, R.C. Davis, J.R. Bargar, J.K. Nørskov, A. Nilsson, A.T. Bell, Identification of highly active Fe sites in (Ni, Fe) OOH for electrocatalytic water splitting, J. Am. Chem. Soc. 137 (2015) 1305–1313.

[8] L. Gong, X.Y.E. Chng, Y. Du, S. Xi, B.S. Yeo, Enhanced catalysis of the electrochemical oxygen evolution reaction by iron (III) ions adsorbed on amorphous cobalt oxide, ACS Catal. 8 (2018) 807–814.

[9] S. Lee, A. Moysiadou, Y.-C. Chu, H.M. Chen, X. Hu, Tracking high-valent surface iron species in the oxygen evolution reaction on cobalt iron (oxy) hydroxides, Energy Environ. Sci. 15 (2022) 206–214.

[10] X. Zheng, B. Zhang, P. De Luna, Y. Liang, R. Comin, O. Voznyy, L. Han, F.P. García de Arquer, M. Liu, C.T. Dinh, T. Regier, J.J. Dynes, S. He, H.L. Xin, H. Peng, D. Prendergast, X. Du, E.H. Sargent, Theory-driven design of high-valence metal sites for water oxidation confirmed using in situ soft X-ray absorption, Nat. Chem. 10 (2018) 149–154.

[11] C.-F. Li, L.-J. Xie, J.-W. Zhao, L.-F. Gu, J.-Q. Wu, G.-R. Li, Interfacial electronic modulation by Fe$_2$O$_3$/NiFe-LDHs heterostructures for efficient oxygen evolution at high current density, Appl. Catal. B Environ. 306 (2022), 121097.

[12] J. Guan, C. Li, J. Zhao, Y. Yang, W. Zhou, Y. Wang, G.-R. Li, FeOOH-enhanced bifunctionality in Ni$_3$N nanotube arrays for water splitting, Appl. Catal. B Environ. 269 (2020), 118600.

[13] S. Ni, H. Qu, Z. Xu, X. Zhu, H. Xing, L. Wang, J. Yu, H. Liu, C. Chen, L. Yang, Interfacial engineering of the NiSe$_2$/FeSe$_2$ p-p heterojunction for promoting oxygen evolution reaction and electrocatalytic urea oxidation, Appl. Catal. B Environ. 299 (2021), 120638.

[14] G. Wang, Y. Tong, K. Li, P. Chen, Heterostructure engineering of iridium species on nickel/molybdenum nitride for highly-efficient anion exchange membrane water electrolyzer, J. Colloid Interface Sci. 628 (2022) 306–314.

[15] Y. Tong, P. Chen, L. Chen, X. Cui, Dual vacancies confined in nickel phosphosulfide nanosheets enabling robust overall water splitting, ChemSusChem 14 (2021) 2576–2584.

[16] H. Wang, X. Cheng, Y. Tong, Coupling of ruthenium with hybrid metal nitrides heterostructure as bifunctional electrocatalyst for water electrolysis, J. Colloid Interface Sci. 629 (2023) 155–164.

[17] Q. Sun, Y. Tong, P. Chen, B. Zhou, X. Dong, Universal strategy of bimetal heterostructures as superior bifunctional catalysts for electrochemical water splitting, ACS Sustain. Chem. Eng. 9 (2021) 4206–4212.

[18] D. Liang, C. Lian, Q. Xu, M. Liu, H. Liu, H. Jiang, C. Li, Interfacial charge polarization in Co$_2$P$_2$O$_7$@ N, P co-doped carbon nanocages as Mott-Schottky electrocatalysts for accelerating oxygen evolution reaction, Appl. Catal. B Environ. 268 (2020), 118417.

[19] J. Li, Z. Cui, Y. Zheng, X. Liu, Z. Li, H. Jiang, S. Zhu, Y. Zhang, P.K. Chu, S. Wu, Atomic-layer Fe$_2$O$_3$-modified 2D porphyrinic metal-organic framework for enhanced photocatalytic disinfection through electron-withdrawing effect, Appl. Catal. B Environ. 317 (2022), 121701.

[20] B.H. Suryanto, Y. Wang, R.K. Hocking, W. Adamson, C. Zhao, Overall electrochemical splitting of water at the heterogeneous interface of nickel and iron oxide, Nat. Commun. 10 (2019) 1–10.

[21] X. Zhang, J. Li, Y. Yang, S. Zhang, H. Zhu, X. Zhu, H. Xing, Y. Zhang, B. Huang, S. Guo, Co$_3$O$_4$/Fe$_{0.33}$Co$_{0.66}$P interface nanowire for enhancing water oxidation catalysis at high current density, Adv. Mater. 30 (2018) 1803551.

[22] C. Zhu, A.L. Wang, W. Xiao, D. Chao, X. Zhang, N.H. Tiep, S. Chen, J. Kang, X. Wang, J. Ding, In situ grown epitaxial heterojunction exhibits high-performance electrocatalytic water splitting, Adv. Mater. 30 (2018) 1705516.

[23] J. Zhao, B. Chen, F. Wang, Shedding light on the role of misfit strain in controlling core–shell nanocrystals, Adv. Mater. 32 (2020) 2004142.

[24] D. Ji, L. Fan, L. Tao, Y. Sun, M. Li, G. Yang, T.Q. Tran, S. Ramakrishna, S. Guo, The kirkendall effect for engineering oxygen vacancy of hollow Co$_3$O$_4$ nanoparticles toward high-performance portable zinc–air batteries, Angew. Chem. Int. Ed. 58 (2019) 13840–13844.

[25] W. Zhou, D. Zhu, J. He, J. Li, H. Chen, Y. Chen, D. Chao, A scalable top-down strategy toward practical metrics of Ni–Zn aqueous batteries with total energy densities of 165 W h kg^{-1} and 506 W h L^{-1}, Energy Environ. Sci. 13 (2020) 4157–4167.

[26] B.D. Anderson, J.B. Tracy, Nanoparticle conversion chemistry: Kirkendall effect, galvanic exchange, and anion exchange, Nanoscale 6 (2014) 12195–12216.

[27] J. Huang, Y. Yan, X. Li, X. Qiao, X. Wu, J. Li, R. Shen, D. Yang, H. Zhang, Unexpected Kirkendall effect in twinned icosahedral nanocrystals driven by strain gradient, Nano Res. 13 (2020) 2641–2649.

[28] M. Kim, H. Seok, N.C.S. Selvam, J. Cho, G.H. Choi, M.G. Nam, S. Kang, T. Kim, P. J. Yoo, Kirkendall effect induced bifunctional hybrid electrocatalyst (Co$_9$S$_8$@MoS$_2$/N-doped hollow carbon) for high performance overall water splitting, J. Power Sources 493 (2021), 229688.

[29] Z. Yang, N. Yang, J. Yang, J. Bergström, M.P. Pileni, Control of the oxygen and cobalt atoms diffusion through Co nanoparticles differing by their crystalline structure and size, Adv. Funct. Mater. 25 (2015) 891–897.

[30] S. Carenco, Y. Hu, I. Florea, O. Ersen, C. Boissière, N. Mézailles, C. Sanchez, Metal-dependent interplay between crystallization and phosphorus diffusion during the synthesis of metal phosphide nanoparticles, Chem. Mater. 24 (2012) 4134–4145.

[31] J.G. Railsback, A.C. Johnston-Peck, J. Wang, J.B. Tracy, Size-dependent nanoscale Kirkendall effect during the oxidation of nickel nanoparticles, ACS Nano 4 (2010) 1913–1920.

[32] R. Nakamura, D. Tokozakura, H. Nakajima, J.-G. Lee, H. Mori, Hollow oxide formation by oxidation of Al and Cu nanoparticles, J. Appl. Phys. 101 (2007), 074303.

[33] Y. Yin, R.M. Rioux, C.K. Erdonmez, S. Hughes, G.A. Somorjai, A.P. Alivisatos, Formation of hollow nanocrystals through the nanoscale Kirkendall effect, Science 304 (2004) 711–714.

[34] Z. Yang, N. Yang, M.-P. Pileni, Nano Kirkendall effect related to nanocrystallinity of metal nanocrystals: influence of the outward and inward atomic diffusion on the final nanoparticle structure, J. Phys. Chem. C 119 (2015) 22249–22260.

[35] V.P. Zhdanov, Kinetic model of oxidation of metal nanoparticles: Cabrera-Mott and Kirkendall effects, Surf. Sci. 684 (2019) 24–27.

[36] X. Li, Z. Kou, J. Wang, Manipulating interfaces of electrocatalysts down to atomic scales: fundamentals, strategies, and electrocatalytic applications, Small Methods 5 (2021) 2001010.

[37] R. Xiang, L. Peng, Z. Wei, Tuning interfacial structures for better catalysis of water electrolysis, Chem. Eur. J. 25 (2019) 9799–9815.

[38] P.P. Dholabhai, B.P. Uberuaga, Beyond coherent oxide heterostructures: atomic-scale structure of misfit dislocations, Adv. Theory Simul. 2 (2019) 1900078.

[39] B.P. Uberuaga, P.P. Dholabhai, G. Pilania, A. Chen, Semicoherent oxide heterointerfaces: Structure, properties, and implications, APL Mater. 7 (2019), 100904.

[40] M.H. Oh, M.G. Cho, D.Y. Chung, I. Park, Y.P. Kwon, C. Ophus, D. Kim, M.G. Kim, B. Jeong, X.W. Gu, J. Jo, J.M. Yoo, J. Hong, S. McMains, K. Kang, Y.-E. Sung, A. P. Alivisatos, T. Hyeon, Design and synthesis of multigrain nanocrystals via geometric misfit strain, Nature 577 (2020) 359–363.

[41] G.H. Choi, M.G. Nam, S.J. Kwak, S.H. Kim, H. Chang, C.-S. Shin, W.B. Lee, P.J. Yoo, Modularly aromatic-knit graphitizable phenolic network as a tailored platform for electrochemical applications, Energy Environ. Sci. 14 (2021) 3203–3215.

[42] D. Li, E.J. Park, W. Zhu, Q. Shi, Y. Zhou, H. Tian, Y. Lin, A. Serov, B. Zulevi, E. D. Baca, C. Fujimoto, H.T. Chung, Y.S. Kim, Highly quaternized polystyrene ionomers for high performance anion exchange membrane water electrolysers, Nat. Energy 5 (2020) 378–385.

[43] W. Chen, M. Mandal, G. Huang, X. Wu, G. He, P.A. Kohl, Highly conducting anion-exchange membranes based on cross-linked poly (norbornene): ring opening metathesis polymerization, ACS Appl. Energy Mater. 2 (2019) 2458–2468.

[44] A. Khataee, A. Shirole, P. Jannasch, A. Krüger, A. Cornell, Anion exchange membrane water electrolysis using Aemion™ membranes and nickel electrodes, J. Mater. Chem. A 10 (2022) 16061–16070.

[45] S. Anantharaj, S. Ede, K. Karthick, S.S. Sankar, K. Sangeetha, P. Karthik, S. Kundu, Precision and correctness in the evaluation of electrocatalytic water splitting: revisiting activity parameters with a critical assessment, Energy Environ. Sci. 11 (2018) 744–771.

[46] J. Kibsgaard, C. Tsai, K. Chan, J.D. Benck, J.K. Nørskov, F. Abild-Pedersen, T. F. Jaramillo, Designing an improved transition metal phosphide catalyst for

[47] hydrogen evolution using experimental and theoretical trends, Energy Environ. Sci. 8 (2015) 3022–3029.

[47] R. Zhang, X. Wang, S. Yu, T. Wen, X. Zhu, F. Yang, X. Sun, X. Wang, W. Hu, Ternary NiCo$_2$P$_x$ nanowires as pH-universal electrocatalysts for highly efficient hydrogen evolution reaction, Adv. Mater. 29 (2017) 1605502.

[48] X.-D. Wang, Y.-F. Xu, H.-S. Rao, W.-J. Xu, H.-Y. Chen, W.-X. Zhang, D.-B. Kuang, C.-Y. Su, Novel porous molybdenum tungsten phosphide hybrid nanosheets on carbon cloth for efficient hydrogen evolution, Energy Environ. Sci. 9 (2016) 1468–1475.

[49] S. Anantharaj, P.E. Karthik, S. Noda, The significance of properly reporting turnover frequency in electrocatalysis research, Angew. Chem. Int. Ed. 60 (2021) 2–19.

[50] J. Kim, P.-C. Shih, K.-C. Tsao, Y.-T. Pan, X. Yin, C.-J. Sun, H. Yang, High-performance pyrochlore-type yttrium ruthenate electrocatalyst for oxygen evolution reaction in acidic media, J. Am. Chem. Soc. 139 (2017) 12076–12083.

[51] R.R. Rao, S. Corby, A. Bucci, M. García-Tecedor, C.A. Mesa, J. Rossmeisl, S. Giménez, J. Lloret-Fillol, I.E.L. Stephens, J.R. Durrant, Spectroelectrochemical analysis of the water oxidation mechanism on doped nickel oxides, J. Am. Chem. Soc. 144 (2022) 7622–7633.

[52] P. Giannozzi, S. Baroni, N. Bonini, M. Calandra, R. Car, C. Cavazzoni, D. Ceresoli, G.L. Chiarotti, M. Cococcioni, I. Dabo, A.D. Corso, S.D. Gironcoli, S. Fabris, G. Fratesi, R. Gebauer, U. Gerstmann, C. Gougoussis, A. Kokalj, M. Lazzeri, L. Martin-Samos, N. Marzari, F. Mauri, R. Mazzarello, S. Paolini, A. Pasquarello, L. Paulatto, C. Sbraccia, S. Scandolo, G. Sclauzero, A.P. Seitsonen, A. Smogunov, P. Umari, P.M. Wentzcovitch, QUANTUM ESPRESSO: a modular and open-source software project for quantum simulations of materials, J. Phys. -Condens. Matter 21 (2009), 395502.

[53] J.P. Perdew, K. Burke, M. Ernzerhof, Generalized gradient approximation made simple, Phys. Rev. Lett. 77 (1996) 3865.

[54] P.E. Blöchl, Projector augmented-wave method, Phys. Rev. B 50 (1994) 17953.

[55] G. Kresse, D. Joubert, From ultrasoft pseudopotentials to the projector augmented-wave method, Phys. Rev. B 59 (1999) 1758.

[56] H.J. Monkhorst, J.D. Pack, Special points for Brillouin-zone integrations, Phys. Rev. B 13 (1976) 5188.

[57] I.C. Man, H.Y. Su, F. Calle-Vallejo, H.A. Hansen, J.I. Martínez, N.G. Inoglu, J. Kitchin, T.F. Jaramillo, J.K. Nørskov, J. Rossmeisl, Universality in oxygen evolution electrocatalysis on oxide surfaces, ChemCatChem 3 (2011) 1159–1165.

[58] X. Cui, P. Ren, D. Deng, J. Deng, X. Bao, Single layer graphene encapsulating non-precious metals as high-performance electrocatalysts for water oxidation, Energy Environ. Sci. 9 (2016) 123–129.

[59] K. Reuter, M. Scheffler, Composition, structure, and stability of RuO$_2$ (110) as a function of oxygen pressure, Phys. Rev. B 65 (2001), 035406.

[60] I.V. Pushkareva, M.A. Solovyev, S.I. Butrim, M.V. Kozlova, D.A. Simkin, A. S. Pushkarev, On the operational conditions' effect on the performance of an anion exchange membrane water electrolyzer: electrochemical impedance spectroscopy study, Membranes 13 (2023) 192.

[61] A. Alobaid, C. Wang, R.A. Adomaitis, Mechanism and kinetics of HER and OER on NiFe LDH in an alkaline electrolyte, J. Electrochem. Soc. 165 (2018) J3395.

[62] Y.S. Park, J. Jeong, Y. Noh, M.J. Jang, J. Lee, K.H. Lee, D.C. Lim, M.H. Seo, W. B. Kim, J. Yang, S.M. Choi, Commercial anion exchange membrane water electrolyzer stack through non-precious metal electrocatalysts, Appl. Catal. B Environ. 292 (2021), 120170.

[63] A. Meena, P. Thangavel, D.S. Jeong, A.N. Singh, A. Jana, H. Im, D.A. Nguyen, K. S. Kim, Crystalline-amorphous interface of mesoporous Ni$_2$P@ FePO$_x$H$_y$ for oxygen evolution at high current density in alkaline-anion-exchange-membrane water-electrolyzer, Appl. Catal. B Environ. 306 (2022), 121127.